

Development of a Photonic Switch via Electro-Capillarity-Induced Water Penetration Across a 10-nm Gap

Eui-Sang Yu, Kyomin Chae, Taehyun Kim, Jongsu Lee, Jungmok Seo, In Soo Kim, Aram J. Chung, Sin-Doo Lee, and Yong-Sang Ryu*

With narrow and dense nanoarchitectures increasingly adopted to improve optical functionality, achieving the complete wetting of photonic devices is required when aiming at underwater molecule detection over the water-repellent optical materials. Despite continuous advances in photonic applications, real-time monitoring of nanoscale wetting transitions across nanostructures with 10-nm gaps, the distance at which photonic performance is maximized, remains a chronic hurdle when attempting to quantify the water influx and molecules therein. For this reason, the present study develops a photonic switch that transforms the wetting transition into perceivable color changes using a liquid-permeable Fabry–Perot resonator. Electro-capillary-induced Cassie-to-Wenzel transitions produce an optical memory effect in the photonic switch, as confirmed by surface-energy analysis, simulations, and an experimental demonstration. The results show that controlling the wetting behavior using the proposed photonic switch is a promising strategy for the integration of aqueous media with photonic hotspots in plasmonic nanostructures such as biochemical sensors.

1. Introduction

Following the discovery of the lotus effect,^[1] numerous nature-inspired micro- and nanostructures have been proposed to control wetting behavior, including hydrophobic water repellency and hydrophilic water affinity,^[2] because they can be used to enhance the understanding of the wetting–dewetting transition.^[3] Advances in surface engineering have allowed the physicochemical functionalization of various surfaces, which in turn provides flexibility in the manipulation of wetting behavior. Thus, investigating the sustainability and stability of water on various surfaces with controlled wetting behavior has generated significant interest due to its importance for fundamental science and potential for use in a variety of industrial applications, including self-cleaning,^[4] fouling, corrosion, and icing protection,^[5] and water collection.^[6]

With advances in nanotechnology, the integration of photonic devices with non-solid media for biochemical sensing applications has become an emerging field in photonics due to its uniqueness of molecular detectability using amplified light–matter interactions.^[7] In particular, with the help of plasmofluidic/optofluidic systems,^[8] imaging systems,^[9] and sensor devices,^[10] significant near-field enhancement within a confined geometry allows for label-free molecular detection at extremely low concentrations. For example, it is possible to detect molecules in femto- to attomolar solutions by concentrating the target molecules in the vicinity of optically functional spots, known as optical hotspots, at the evaporation front.^[11] Given that narrower and more closely packed nanostructures such as gaps, pores, cavities, and bow-ties are more likely to confine the near-field resonance,^[12] water-based molecular analysis using a photonic surface needs to overcome the high degree of water repellency that arises from the nanogeometry of photonic devices and the strong surface tension of water molecules. The surface roughness of a nanogeometry on a sub-100 nm scale has been reported to produce high water repellency;^[13] thus, ensuring the complete wetting of photonic surfaces with ultrafine complex geometries is an essential prerequisite for achieving underwater molecular analysis using photonic devices.

A wide range of techniques has been employed to fully wet nanogeometries, including the use of highly hydrophilic

E.-S. Yu, J. Lee, S.-D. Lee
Department of Electrical and Computer Engineering
Seoul National University
Seoul 08826, Republic of Korea

E.-S. Yu, T. Kim, J. Lee, Y.-S. Ryu
Brain Science Institute
Korea Institute of Science and Technology
Seoul 02792, Republic of Korea
E-mail: ysyu82@kist.re.kr

K. Chae, J. Seo
School of Electrical and Electronic Engineering
Yonsei University
Seoul 03722, Republic of Korea

I. S. Kim
Nanophotonics Research Center
Korea Institute of Science and Technology
Seoul 02792, Republic of Korea

A. J. Chung
School of Biomedical Engineering
Korea University
Seoul 02841, Republic of Korea

Y.-S. Ryu
KU-KIST Graduate School of Converging Science and Technology
Korea University
Seoul 02481, Republic of Korea

 The ORCID identification number(s) for the author(s) of this article can be found under <https://doi.org/10.1002/sml.202107060>.

DOI: 10.1002/sml.202107060

materials,^[14] surface treatments,^[15] and controlled solvent conditions.^[16] However, the in situ monitoring of how and when water wets optical hotspots remains difficult. In particular, understanding the mechanisms underlying the infiltration of bulk water into ultra-narrow nanogeometries and realizing tunable photonic devices that can transduce changes in the wetting conditions into optical signals are required to develop extremely sensitive bio-photonic devices. In this respect, the development of an ideal platform for photonic switches that can track nanoscale dynamic wetting transitions and for photonic detectors that allow the quantitative analysis of the stages of wetting is vital.

Herein, we propose an electro-capillary-induced photonic switch that visualizes Cassie-to-Wenzel transitions using changes in color. A liquid-permeable Fabry–Perot resonator (FPR), consisting of a metal–dielectric–metal tri-layer with a perforated top layer and an etched dielectric spacer,^[17] was designed to evaluate the movement of external water into the dielectric space of the photonic switch. Electrically controlled wetting transitions in the FPR followed by remarkable shifts in the resonance confirmed the infiltration of water across the 10-nm gap and the in situ colorimetric monitoring of the wetting state with the permeation of water. In addition to elucidating the mechanisms underlying the wetting transitions, the quantification of underwater glucose was demonstrated as an example of a refractive index (RI) sensing and a photonic switch.

2. Result

2.1. Design of the Liquid-Permeable FPR and Optical Characterization

For the in situ monitoring of wetting states using changes in color, liquid-permeable FPRs with ultra-narrow nanogaps were prepared (Figure 1a and Methods). Tri-layered FPR chips have been reported to exhibit a shift in the spectral resonance position (λ_{res}) with respect to physicochemical changes (thickness and refractive index) in the constituent dielectrics, leading to visible changes in color.^[17] A 150-nm-thick hydrophobic perfluoro-(butenyl vinyl ether) (PBVE) optical spacer was spin-coated onto a 120-nm-thick gold (Au) mirror that had been deposited on a substrate. Deposition of a 30-nm-thick Au film using low-density nucleation on the PBVE surface resulted in the uniform self-assembly of inter-connected Au nanoparticles over a large area as shown in the scanning electron microscopy (SEM) image (Figure 1b). Finally, O₂ plasma treatment partially etched away the underlying PBVE through the nanogaps in the overlying Au film, leaving behind PBVE nanopillars and hollow voids (Figure 1c). Because the optical properties of FPRs are highly dependent on the RI (n) of the dielectrics, different etching durations (0, 20, 40, and 60 s for FPRs I, II, III, and IV, respectively) were used to adjust the optical resonance by tailoring an effective RI (n_{eff}). The spectral resonance positions in reflectance spectra were blue-shifted from 639 to 613, 578,

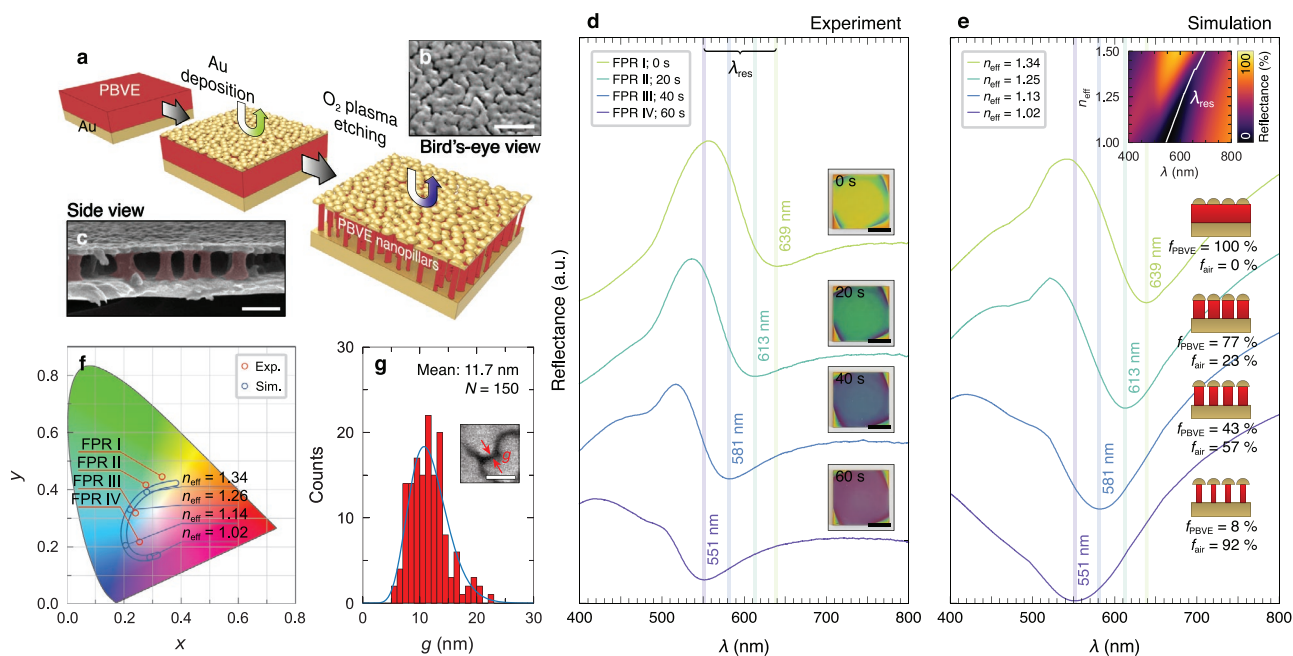


Figure 1. Fabrication and optical characterization of FPRs. a–c) Schematic illustration of the fabrication process for the FPR (a) that produces a top Au layer with nanogaps (b, top-view SEM image) and a spacer layer with PBVE nanopillars and air voids (c, side-view SEM image). d,e) Reflectance spectra for FPR samples with different etching durations (d, inset: photographic images of the samples) and corresponding simulation curves (e, inset: graph for simulated reflectance spectra as a function of n_{eff} and images for the cross-sectional schematics of the FPRs); light-green, green, blue, and purple for FPRs I, II, III, and IV, respectively. f) CIE 1931 color chromaticity diagram marked with experimental (red dots) and simulated spectra (blue dots) from FPRs with different etching durations. g) Width distribution histogram of the inter-particulate gaps in the top Au layer (blue line for gamma distribution approximation; inset: SEM image). Scale bars: 200 nm (b,c), 1 cm (d), and 40 nm (g).

and 551 nm as the etching time increased, thus producing a distinctive light green, green, blue, and purple color, respectively (Figure 1d and normalized reflectance for Figure S1a in Note S1, Supporting Information). According to Bruggeman's effective medium theory (BEMT),^[18] binary composite layers (i.e., the top and dielectric layer each) in the FPR entangled on a subwavelength scale can be treated as a macroscopically homogeneous film. Thus, the effective dielectric constant (ϵ_{eff}) of each layer is expressed by

$$f_1 \frac{\epsilon_1 - \epsilon_{\text{eff}}}{\epsilon_1 + \kappa \epsilon_{\text{eff}}} + f_2 \frac{\epsilon_2 - \epsilon_{\text{eff}}}{\epsilon_2 + \kappa \epsilon_{\text{eff}}} = 0 \quad (1)$$

where κ , ϵ_1 , ϵ_2 , f_1 , and f_2 represent the screening parameter ($\kappa = 1$ for a semi-continuous metal film), dielectric constant, and volume fraction for the two entangled materials ($f_1 + f_2 = 1$). By matching measurements and simulations, n_{eff} of FPRs I, II, III, and IV was calculated to be 1.34, 1.25, 1.13, and 1.02, with the PBVE nanopillars occupying 100%, 77%, 43%, and 8% of the optical spacer, respectively (Figure 1e and normalized reflectance for Figure S1b in Note S1, Supporting Information). The n_{eff} of the optical spacer varies with the etching time, which determines the volume fraction of the PBVE nanopillars (f_{PBVE}) and air voids ($f_{\text{air}} = 1 - f_{\text{PBVE}}$) (Figure S2 in Note S1, Supporting Information). Thus, reducing f_{PBVE} ($n_{\text{PBVE}} = 1.34$) results in an increase in f_{air} ($n_{\text{air}} = 1.00$), decreasing the n_{eff} of the spacer and blue-shifting λ_{res} .

To analyze the colorimetric properties, the spectra were marked on the CIE 1931 color chromaticity diagram (Figure 1f). Despite a slight mismatch, similar trends in the measurements and simulations indicated that the electromagnetic responses of the theoretical model based on BEMT approximation accurately described the change in the color of the device. In addition, a large number ($N = 150$) of randomly chosen gap distances (g) was analyzed to produce a gamma distribution approximation with a mean of 11.7 nm (Figure 1g), confirming that the nanogaps of the top Au film were ultra-narrow. Therefore, hydrophobic characteristics arise in this ultra-fine nanomorphology and the hydrophobic material underneath, rendering the spacer region underneath impervious to water.

2.2. Surface Energy Analysis of Electrically Induced Wetting Transitions

Water droplets on micro- or nanostructured surfaces can exist in three types of wetting state: Cassie, intermediate, and Wenzel states. A Cassie state is a heterogeneous wetting state in which the water sits on the surface of the nanostructures with air pockets trapped underneath.^[19] During the wetting transition, water partially wets the underlying micro/nanostructures of the solid surface to create an intermediate state, then the entire air pocket is replaced by water to produce a Wenzel state.^[20] However, because the free energy of the intermediate state (E_{inter}) is higher than that of the Cassie state (E_{Cassie}), the wetting transition from a metastable Cassie state to a stable Wenzel state requires external energy to reduce the energy barrier (ΔE), with $\Delta E = E_{\text{inter}} - E_{\text{Cassie}}$ (Figure 2a). This indicates that applying an external stimulus so that $\Delta E = 0$ will lead to a spontaneous

Cassie-to-Wenzel transition. Practically, a transition in wetting states on the FPR platform can be achieved by applying electrical potential because the charge accumulation in the top Au layer modulates the surface tension at the solid-liquid (s-l) interface with an applied voltage across the water droplet. The surface free energy (E) of a droplet with the application of an electrical field can be obtained using

$$E = A_{\text{lv}}\gamma_{\text{lv}} + A_{\text{sv}}\gamma_{\text{sv}} + A_{\text{sl}}(\gamma_{\text{sl}} - \eta\gamma_{\text{lv}}) \quad (2)$$

where A_{lv} , A_{sv} , A_{sl} , γ_{lv} , γ_{sv} , γ_{sl} , and η are the interfacial area (A) and surface tension (γ) of the liquid-vapor (l-v), solid-vapor (s-v), and s-l interfaces, and a dimensionless electrowetting number that indicates the ratio of the electrostatic energy to the l-v interfacial energy, respectively.

To determine E_{C} and E_{inter} of a water droplet using Equation (2), the physical parameters γ , A , and η need to be acquired. For a droplet on a rough solid surface under an applied voltage (V), the droplet contact angle (θ_c) is given by the extended Lippman-Young equation combined with Cassie-Baxter model:^[21]

$$\cos \theta_c = R f_{\text{sl}} (\cos \theta_0 + \eta) - f_{\text{lv}} \quad (3)$$

where θ_0 , R , f_{sl} , and f_{lv} denote contact angle on a smooth surface, surface roughness factor, area fractions of s-l and l-v interfaces, respectively. Since Equation (3) demonstrates that η can be estimated from electrowetting contact angle, electrowetting characteristics with an increase in V were monitored via the measurement of θ_c of an 8- μL water droplet placed on FPRs with different etching durations (Figure 2b). By applying DC voltage at increasing amplitudes, θ_c of the FPRs gradually decreased before leveling off,^[22] while the more heavily etched FPRs displayed greater changes in θ_c (Figure 2c). As an essential step to describe dynamic wetting transitions on the FPR IV, the re-entrant mushroom-structured model introduced by Garimella's group^[23] (Figure 2d and Figure S3 in Note S2, Supporting Information; $P = 100$ nm, $D = 90$ nm, $d = 30$ nm, $H = 170$ nm, and $h = 25$ nm) was adopted to quantify the interfacial areas of the droplet in the Cassie (Figure 2e) and intermediate states (Figure 2f). On this model of rough heterogeneous surface with air fractions (Figure S4a in Note S3, Supporting Information), the effective η of the FPR IV was retrieved using the extended Lippman-Young equation (Figure S4b in Note S3, Supporting Information). Unlike Garimella's model, our FPR platform consists of a heterogeneous solid interface that produced distinct A and γ values for the constituent materials (i.e., PBVE as the dielectric film and Au as the top/bottom film). Thus, the heterogeneity of the solid interfaces must be considered using different values for A and γ (Supporting Note 4) to obtain E_{Cassie} and E_{inter} from Equation (2), which are essential to evaluate ΔE under the application of potential (Figure S5 in Note S5, Supporting Information). Theoretical analysis indicated that the Cassie-to-Wenzel energy barrier for FPR IV decreased with a higher potential and that the surface energy of the s-l interface played a significant role in wetting transitions (Figure S6 in Note S6, Supporting Information). Consequently, the Cassie-to-Wenzel

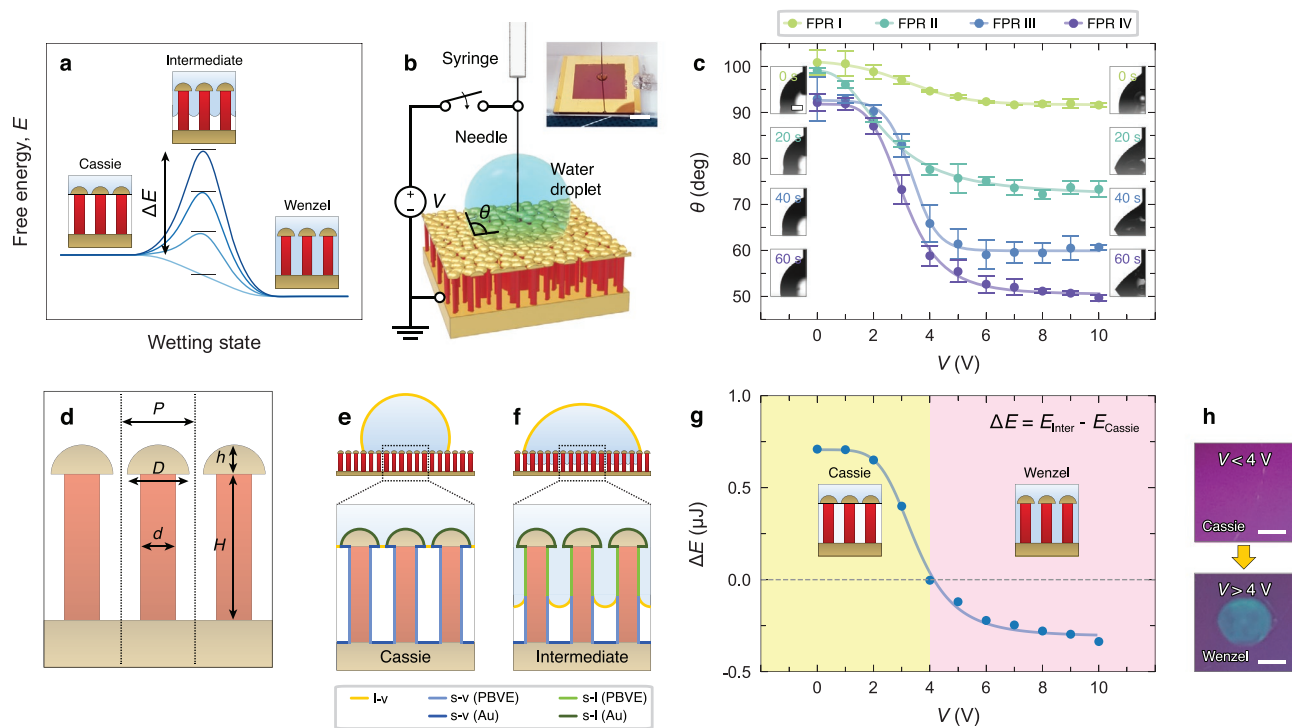


Figure 2. Surface energy analysis of wetting transitions on the FPR. a) Conceptual diagram of the surface free energy for the Cassie-to-Wenzel transition. b) Schematic illustration of the setup for contact angle measurement (inset: photograph of the experimental setup). c) Contact angle as a function of the applied voltage on FPRs with different etching durations (inset: micrographs of droplets at 0 [left] and 10 V [right]). d–f) Geometric model for surface energy analysis (d) and interfacial components in the Cassie (e) and intermediate state (f); yellow, light blue, light green, dark blue, and dark green for the l-v, s-v (PBVE), s-l (PBVE), s-v (Au), and s-l (Au) interfaces, respectively. g) Calculated energy barrier for the Cassie-to-Wenzel transition as a function of applied voltage (inset: corresponding wetting schematics). h) Experimental photographs of FPR IV before and after applying 4 V across the droplet. Scale bars: 5 mm (b), 200 μm (c), and 0.5 mm (h).

transition on FPR IV was expected to be initiated with a transition voltage of 4 V, for which ΔE would become zero (Figure 2g). This theoretical approach was substantiated by observing the change in color after applying voltages across the droplet on the FPR IV that were higher than the transition voltage ($V > 4$ V; Figure 2h). The excellent correspondence between the theoretical analysis and experimental results confirmed that wetting transitions on the FPRs can be predicted qualitatively.

2.3. Nanoscale Monitoring of Wetting Transitions Inside the Nanomorphological Structure

After theoretically establishing the Cassie-to-Wenzel transition using the surface energy model, experiments were conducted to verify the in situ optical monitoring of dynamic wetting behavior, that is, the Cassie-to-Wenzel transition. A water layer was encapsulated between FPR IV and indium-tin-oxide (ITO)-coated glass using a polydimethylsiloxane (PDMS) spacer (Figure 3a and Figure S7 in Note S7, Supporting Information). Before applying the voltage, the structure retained its original purple color, which indicated that the water was present in a Cassie state. The application of 4 V for 1 s turned the color green, and this was maintained even when the voltage was removed (Movie S1, Supporting Information), demonstrating that a Cassie-to-Wenzel transition had occurred. This was

attributed to the higher energy barrier for the Wenzel-to-Cassie transition than for the Cassie-to-Wenzel transition. Thereby, the maintenance of a homogeneous Wenzel state provides an optical memory effect until the water trapped in the dielectric space has been completely evaporated (Figure 3b). Note that ITO glass was disassembled from the samples to evaporate water, maintaining the Wenzel state during the water drying process.

To quantitatively analyze the dynamic wetting behavior with the application of voltage, reflection spectra were measured at intervals of 0.2 s. The electrically triggered penetration of water across the 10-nm gaps led to $\Delta\lambda_{\text{res}} = 87$ nm (544 to 631 nm) within 0.6 s (Figure 3c and normalized reflectance for Figure S8a in Note S7, Supporting Information), indicating that a significant increase in the RI occurred in the spacer region. Judging from the corresponding simulation results (Figure 3d and normalized reflectance for Figure S8b in Note S7, Supporting Information), the spectral shift of λ_{res} ($\Delta\lambda_{\text{res}}$) on FPR IV ($f_{\text{PBVE}} = 0.08$, $f_{\text{air}} = 0.92$, and $f_{\text{water}} = 0$) from 544 to 631 nm ($\Delta\lambda_{\text{res}} = 87$ nm) can be interpreted as an increase in n_{eff} from 1.02 to 1.34, indicating that the electrically induced wetting transition replaced the pre-existing air pockets with water to a level of $f_{\text{air}} = 0$ and $f_{\text{water}} = 0.92$ (Figure S9 in Note S7, Supporting Information). The color diagram for n_{eff} presented as the inset in Figure 3d illustrates that the water influx via electrowetting can be quantified using perceivable changes in color. Overall,

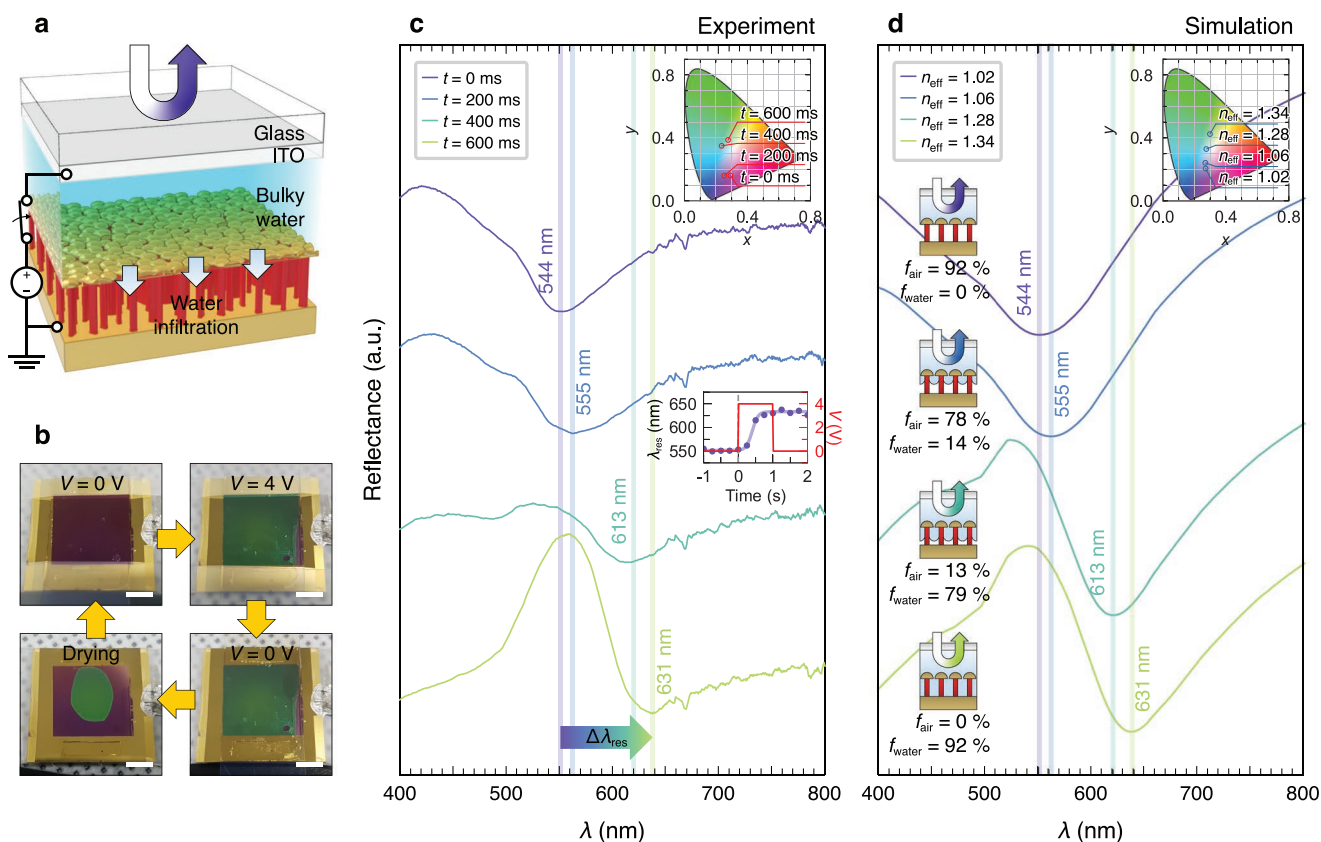


Figure 3. In situ optical monitoring of the Cassie-to-Wenzel transition on the FPR. a) Schematic illustration of the in situ optical monitoring of the wetting transition under an electro-potential. b) Photographs of the FPR's reversible color changes above the transition voltage reflecting the wetting states; purple for a Cassie state and green for a Wenzel state. c,d) Reflectance spectra under an electrically induced Cassie-to-Wenzel transition (c; inset: CIE 1931 color chromaticity diagram marked with the experimental time-lapse spectra and graph of spectral position of λ_{res} in response to 1 s of 4 V DC voltage) and corresponding simulation curves (d; inset: CIE 1931 color chromaticity diagram marked with simulated time-lapse spectra and schematics for the cross-section of the FPR). Scale bars: 5 mm (b).

the water occupancy equilibrium within the dielectric layer allowed the qualitative monitoring of the wetting stages and the quantitative analysis of the degree of wetting inside the dielectric materials. In particular, it was possible to produce a photonic switch with an optical memory effect due to the energetic stability of the Wenzel state, and this behavior can be applied to advanced tunable photonic devices such as reflective displays, color filters, and optical anti-counterfeiting devices.

2.4. Application of a Photonic Switch Based on Electrically Induced Wetting Transitions

To produce switchable photonic devices for real-world applications, several factors should be considered, including their fabrication, cost-effectiveness, performance, and amenability to system integration. In particular, a facile single-step technique employing cost-effective nanofabrication techniques that are amenable to the large-scale production of plasmonic devices is strongly desirable. Therefore, the feasibility of reconfigurable photonic switches was examined. As an example, the tunable encryption/decryption of an optical message was tested via patterned etching of the underlying dielectric film (Figure 4a,b)

or site-selectively controlled liquid influx (Figure 4c,d). The informational message was inscribed using site-selective etching for 60 s through a patterned shadow mask and assembled with ITO glass (Figure 4a), resulting in a recognizable FPR IV pattern showing purple-colored 'KIST' surrounded by a non-etched green-colored FPR I background region (upper image in Figure 4b). Electrically induced liquid permeation into the etched dielectric area resulted in the message being hidden (lower image in Figure 4b) due to the RI matching between PBVE ($n_{\text{PBVE}} = 1.34$) and water ($n_{\text{water}} = 1.34$). The message was also displayed via site-selective liquid permeation into the optical spacer using patterned ITO (Figure 4c). In this process, the FPR IV sample was assembled with a glass substrate with the transparent ITO pattern "KIST" (upper image in Figure 4d and Figure S10 in Note S8, Supporting Information). The site-selective liquid penetration immediately below the patterned ITO electrode displayed clear information when the voltage was applied (lower of Figure 4d). Note that we applied 5 V for all of the experiments.

Finally, direct colored writing through site-selective control was examined using a customized setup for the accurate re-localization of the needle (Figure 4e). The blunt needle was connected to motorized linear stages and computer-controlled

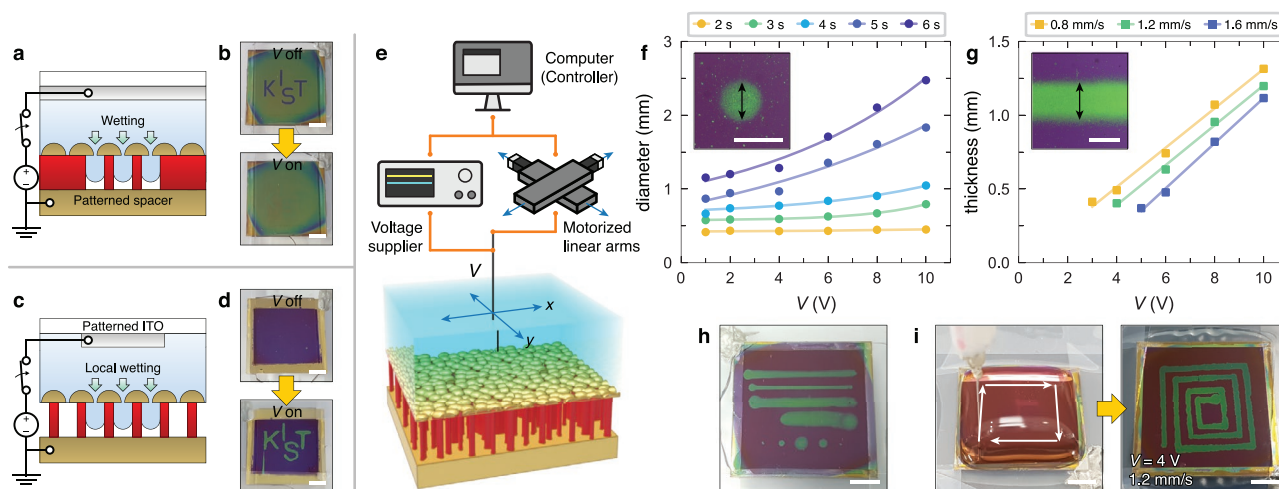


Figure 4. Site-selective wetting transitions on FPRs for dynamic photonic switch applications. a–d) Schematic illustrations (a,c) and experimental results (b,d) for dynamic photonic switch encryption (a,b; patterned dielectric etching) and decryption (c,d; patterned ITO electrode) through site-selective wetting transitions. e–i) Schematic illustration of the setup for direct colored writing using site-selective wetting transitions (e; re-localizable needle over the FPR) and experimental results in the form of dots (f) and lines (g) as a function of the engineered variables (moving speed, voltage amplitude, and applying duration), resulting in various pattern sizes (h) and shapes (i). Scale bars: 5 mm (b,d,f,g) and 0.5 mm (h,i).

voltage sources, submerged in water, and kept 100 μm apart from the sample. The applied voltage and movement were systematically controlled by a computer. The localized wetting transition by applying voltages led to the formation of dot-shaped colors. As the amplitude or duration of applying voltages increases, their diameter (d) is widened from 415 μm to 2.47 mm since the localized wetting transition spread through sideways within the dielectric spacer (Figure 4f and Movie S2, Supporting Information). By moving the motorized stage in a linear direction, line-shaped colors were observed, and their width also widened from 403 μm to 1.31 mm as the voltage increased or the moving speed decreased (Figure 4g). The minimum feature sizes (400- μm -width lines or dots) were comparable to the external diameter of the blunt needle (400 μm for a 27G needle), which indicates that a much finer resolution can be achieved by utilizing a sharper needle. Based on the results, structural colors with numerous arbitrary geometric shapes can be realized in combinations of dots and lines because these are essential design elements (Figure 4h,i, and Movie S3, Supporting Information).

2.5. Colorimetric Detection of Molecular Concentrations via Electrically Induced Wetting Transitions

Due to its close association with disease and metabolism, glucose has been regarded as a representative target analyte in optical sensor research.^[24] We tested whether suspended glucose could also penetrate the 10-nm gaps when water permeated toward the dielectric layer and whether the resultant spectral shifts could be used to identify the molecular concentration using our FPR platform. For this purpose, four FPR IV regions prepared using soft-lithographic PDMS stamping (Figure S11 in Note S8, Supporting Information) were exposed to different concentrations of glucose ($C = 0, 10, \text{ and } 20 \text{ wt.}\%$) dissolved in water. After applying 4 V for 1 s, the original purple colors

turned into different colors depending on the glucose concentration; specifically, dark green, green, and light green for $C = 0, 10, \text{ and } 20 \text{ wt.}\%$, respectively (Figure 5b). Note that the colors and reflective spectra were measured and analyzed at identical angles to exclude the effects of angular dependency. SEM images after water evaporation displayed different amounts of glucose deposition (the green pseudo-color in Figure 5c) inside the dielectric region. The measured spectral shifts of λ_{res} provided quantitative information based on the RI of the glucose solution (n_{soln}) within the optical spacer and could thus be used to identify the glucose concentration within the solution. Compared with the shift of $\Delta\lambda_{\text{res}} = 88 \text{ nm}$ (from 545 to 633 nm) from pure water ($C = 0 \text{ wt.}\%$), the larger shift of $\Delta\lambda_{\text{res}} = 95$ and 101 nm (from 545 to 640 and 646 nm) retrieves RI of solution to be $n_{\text{soln}} = 1.346$ and 1.364, respectively (Figure 5d). The good correspondence between the experimentally estimated values and literature values^[25] ($n_{\text{soln}} = 1.348$ and 1.363 for $C = 10$ and 20 wt.%; inset of Figure 5d) demonstrates that the spectral shift of the FPR by electrowetting transition can be employed to detect the glucose concentration of a solution.

The marks of experimental/simulated spectra on CIE 1931 color chromaticity diagrams also exhibited similarities between the experimental measurements and simulations depending on the glucose concentration (Figure 5e). Using FPR's color arise from the complete wetting state of pure water ($C = 0 \text{ wt.}\%$) as a standard, color difference (ΔE^*) between each color mark on the CIE diagram and standard color were estimated varying glucose concentration (inset in Figure 5e). Here, ΔE^* is defined as, $\Delta E^* = \sqrt{(\Delta L^*)^2 + (\Delta a^*)^2 + (\Delta b^*)^2}$, where ΔL^* , Δa^* , and Δb^* represent the difference of lightness, red/green, and yellow/blue between two different colors (L^* , a^* , and b^* note for CIELAB coordinates converted from CIE 1931 coordinates). Note that ΔE^* represents a distance between locations of two colors in CIE color space. Thus, ΔE^* is a quantitative index that indicates human cognitive similarity and difference between two different colors. Because observers can distinguish two different colors with the naked

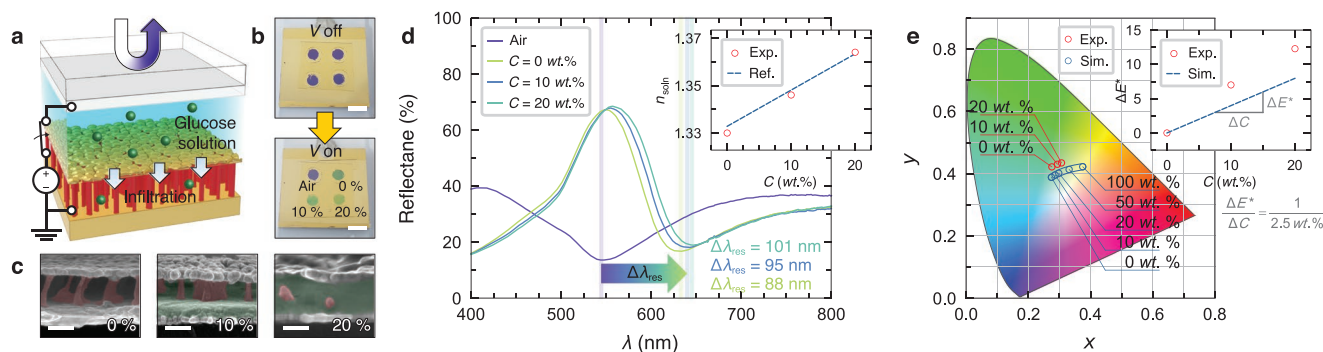


Figure 5. Colorimetric detection of the molecular concentration using a wetting transition. a) Schematic illustration of colorimetric detection for a glucose solution in the dielectric region. b,c) Photographic images of FPR color variation for glucose concentrations of 0, 10, and 20 wt.% (b) and corresponding side-view SEM images of glucose deposition inside the dielectric spacer (c). d) Measured reflectance spectra for different glucose concentrations (inset: n_{soln} from experiment and literature^[25] as a function of glucose concentration). e) CIE 1931 color chromaticity diagram marked with measured (red dots) and simulated colors (blue dots) as a function of the glucose concentration (inset: experimental and simulational ΔE^* as a function of the glucose concentration). Scale bars: 5 mm (b) and 100 nm (c).

eye when $\Delta E^* > 1$,^[26] experimental values of $\Delta E^* = 7.0$ (between $C = 0$ and 10 wt.%) and 12.3 (between $C = 0$ and 20 wt.%) were sufficient to yield perceivable color differences with respect to the glucose concentration (inset in Figure 5e). In particular, concentration difference (ΔC) of $\Delta C = 2.5$ wt.% was the minimum resolution for optical detectability in recognizing color differences because its corresponding color difference becomes $\Delta E^* = 1$ from the simulation slope ($\Delta E^*/\Delta C$). As a result, the high refractive index sensitivity ($323.5 \text{ nm RIU}^{-1}$)^[17a] of the FPR device allowed the colorimetric detection of molecular concentrations in liquids with the naked eye; this can be extended to the precise quantification of the molecular concentration in a solution with the help of simple spectral measurements.

3. Conclusion

A photonic switch that visualizes nanoscale volumetric wetting transitions was proposed in the present study to allow the real-time quantitative monitoring of the water influx and the molecular concentration of a target solute. An electrically induced photonic switch with an optical memory effect was realized on a liquid-permeable FPR device. This was attributed to the high refractive index sensitivity ($323.5 \text{ nm RIU}^{-1}$)^[17a] of the FPR device, which allowed colorimetric detection with the naked eye of the electrowetting behavior of water across 10-nm nanogaps; this can also be used to quantify the molecular concentration of a solution via spectral analysis. Being able to perceive the water influx across a 10-nm gap and to detect molecules by taking advantage of controlled wetting transitions provides a number of opportunities and advantages.

First, electrically induced water infiltration across an ultra-narrow nanogap of 10 nm can provide insights for the development of advanced biochemical photonic sensors by ensuring complete wetting for the access of target analytes to nanoarchitectures. Recent studies have shown that nanoscale surface topographies strongly determine wetting behavior, with sub-100 nm nanotextures exhibiting considerable water repellency.^[13] Because extremely narrow and dense nanoarchitectures have

been developed to improve optical functionalities, the complete wetting of optical hotspot sites is vital when water-repellent optical materials are integrated with an aqueous medium. Because electrowetting is universal in metallic nanostructures, our proposed approach can be adopted for photonic devices at various wavelength regimes, such as surface-enhanced Raman spectroscopy (SERS),^[8a] surface-enhanced infrared absorption (SEIRA),^[27] and terahertz sensing.^[28] By integrating with these spectroscopic techniques that provide molecular vibrational fingerprint information, advanced biochemical photonic sensors with chemical selectivity are expected to go beyond the limit of refractive index sensing.

Second, the proposed FPR-based strategy provides colorimetric visualization of wetting states and detailed information for the internal regions of nanostructures with the assistance of simple spectral measurements. Though considerable efforts have been expended on the real-time monitoring of Cassie-to-Wenzel transitions, no previous methods have been proven capable of tracking the kinetics of wetting transitions and identifying the wetting state inside nanoscale geometries without the use of complicated techniques and high-tech instruments. Conventionally, wetting states have been monitored using contact angle measurements and analyzing the hysteresis.^[29] However, similar contact angles are occasionally measured with different wetting configurations, preventing the precise identification of the wetting state. To overcome this limitation, more accurate microscopic techniques have been developed that employ optical microscopy (OM; confocal^[30] and interference microscopy^[31]) and electron microscopy (EM; environmental,^[32] cryo-SEM,^[33] and polymerizable liquid^[34]). However, EM approaches are difficult to use for the in situ monitoring of dynamic kinetics, while OM approaches are limited in the monitoring of nanoscale wetting. Recently, non-microscopic approaches such as acoustic^[35] and electrochemical techniques^[36] and Fourier transform infrared spectroscopy^[37] have been proposed for the in situ monitoring of wetting inside nanomorphological structures, but they do not offer direct visualization and require expensive equipment. For this reason, the proposed integration of a structural color device with electrowetting offers a robust alternative.

Third, by applying instant low-voltage electric signals, a fast-response photonic switch with optical tunability and a memory effect was realized. To develop reflective displays and advanced photonic devices, conventional structural color printing techniques have led to high-quality information displays using high-tech instruments.^[38] Our methodology allows fast-response and rewritable structural color printing with inexpensive devices. In addition, chip fabrication does not rely on high-tech instruments, allowing for facile fabrication, which increases its potential for use in industrial applications.

Overall, our strategy of employing electrowetting with rewritable photonic nanostructures is expected to create numerous opportunities to clarify the underlying surface physics at the liquid–solid interface of nanomorphological structures and to produce advanced tunable photonic devices and surface-enhanced optical sensor systems.

4. Experimental Section

Fabrication of Liquid-Permeable FPRs: To prepare a liquid-permeable FPR, a bare silicon substrate (2 cm × 2 cm) was cleaned in acetone, isopropyl alcohol, and distilled (DI) water for 20 min each using an ultra-sonicator (JAC-3010, Kodo). A 5-nm-thick titanium adhesion layer and a 120-nm-thick Au bottom mirror were deposited on the cleaned Si substrate using e-beam evaporation (ei-5k, ULVAC). A PBVE polymer solution prepared by mixing 9.0 wt.% CyclAFlo Clear solution (CyclAFlo Clear-Silane, Chromis Technologies) and a perfluorinated solvent (CyclASolv-PFC180, Chromis Technologies) at a weight ratio of 1:1 was then spin-coated onto the Au surface (3000 rpm for 30 s and subsequent thermal annealing at 80°C for 60 min on a hotplate). A 30-nm-thick top Au layer with a self-assembled nanogeometry with 11-nm-wide gaps (Figure 1g) was produced on the 164-nm-thick PBVE surface as an optical spacer using evaporation (10^{-5} Torr, 0.3 \AA s^{-1}) via thermal deposition (MHS-1800, Muhna). Finally, O₂ plasma reactive ion etching (RIE, 100 mTorr, RF power of 150 W, and an O₂ gas flow of 100 sccm; RIE 80 Plus, Oxford Instruments) was conducted to produce PBVE nanopillars and hollow voids in the dielectric region. A patterned shadow mask was used during the etching process for optical encryption.

SEM Measurement: Prior to SEM measurement, the entire surface of the target geometry was covered with a 2-nm-thick platinum layer using an ion sputter coater (E-1045, Hitachi). SEM measurements were then taken using a field-emission SEM (Nova Nano SEM 200, FEI) equipped with a through-lens detector (10 kV, 140 A, working distance of 5 mm). For processing and analysis of the SEM images, ImageJ (National Institutes of Health) was used.

Contact Angle Measurement: Contact angles and droplet images were obtained using the sessile-drop method with a contact angle goniometer (SmartDrop, Femtoblab). In this process, liquid droplets were dispensed onto the surface of the FPR using a syringe equipped with a blunt needle (27G). To observe the variation in the contact angle of an 8- μ L water drop with the application of voltage, a DC voltage source (SDG2122X, SIGLENT) was connected to the needle while the bottom Au film was grounded to the device (Figure 2b). During the measurements, the vertical distance between the needle and the substrate was maintained at about 400 μ m.

Experimental Setup for the Electrically Induced Direct Writing of Structural Color Patterns: After mounting and fixing the FPR substrate onto the stage, the bottom Au film was connected to the ground line of a waveform generator (SDG2122X, SIGLENT). A sufficient amount of DI water was then dispensed onto the surface with a 27G syringe needle dipped into the water and held 100 μ m away from the FPR surface. The needle was connected to a power source and to orthogonally aligned (for x- and y-axial movement) motion stages (SAN45 05/10/20-300S+1SR/2SR/3SR and SAN65 05/10/20-300S+1SR/2SR/3SR,

Science Town). Under the control of a computer, the needle was systematically relocated using customized code based on Labview (National Instruments).

Supporting Information

Supporting Information is available from the Wiley Online Library or from the author.

Acknowledgements

This work was supported by KIST Institutional Programs (No. 2E31512, and 2E31821). Y.-S.R. acknowledges the support from a National Research Foundation of Korea (NRF) grant funded by the Korean government (MSIT) (No. 2021R1A2C2009236) and KU-KIST school project. J.S. acknowledges the support from a National Research Foundation of Korea (NRF) grant funded by the Korean government (MSIT) (no. 2021M3H4A1A03048658).

Conflict of Interest

The authors declare no conflict of interest.

Data Availability Statement

The data that support the findings of this study are available from the corresponding author upon reasonable request.

Keywords

Fabry–Perot resonators, nanogaps, refractive index sensors, tunable structural color, wetting transition

Received: November 22, 2021

Revised: January 18, 2022

Published online:

- [1] W. Barthlott, C. Neinhuis, *Planta* **1997**, *202*, 1.
- [2] a) P. Roach, N. J. Shirtcliffe, M. I. Newton, *Soft Matter* **2008**, *4*, 224; b) L. Feng, S. Li, Y. Li, H. Li, L. Zhang, J. Zhai, Y. Song, B. Liu, L. Jiang, D. Zhu, *Adv. Mater.* **2002**, *14*, 1857.
- [3] P.-G. De Gennes, F. Brochard-Wyart, D. Quéré, *Capillarity and Wetting Phenomena: Drops, Bubbles, Pearls, Waves*, Springer, New York, NY **2004**.
- [4] R. Füstner, W. Barthlott, C. Neinhuis, P. Walzel, *Langmuir* **2005**, *21*, 956.
- [5] a) N. Wang, D. Xiong, Y. Deng, Y. Shi, K. Wang, *ACS Appl. Mater. Interfaces* **2015**, *7*, 6260; b) L. Cao, A. K. Jones, V. K. Sikka, J. Wu, D. Gao, *Langmuir* **2009**, *25*, 12444.
- [6] A. R. Parker, C. R. Lawrence, *Nature* **2001**, *414*, 33.
- [7] a) X. Fan, I. M. White, *Nat. Photonics* **2011**, *5*, 591; b) H. Schmidt, A. R. Hawkins, *Nat. Photonics* **2011**, *5*, 598.
- [8] a) C. Monat, P. Domachuk, B. J. Eggleton, *Nat. Photonics* **2007**, *1*, 106; b) D. Psaltis, S. R. Quake, C. Yang, *Nature* **2006**, *442*, 381; c) P. P. Patra, R. Chikkaraddy, R. P. N. Tripathi, A. Dasgupta, G. V. P. Kumar, *Nat. Commun.* **2014**, *5*, 4357; d) M. Wang, C. Zhao, X. Miao, Y. Zhao, J. Rufo, Y. J. Liu, T. J. Huang, Y. Zheng, *Small* **2015**, *11*, 4423.

- [9] X. Cui, L. M. Lee, X. Heng, W. Zhong, P. W. Sternberg, D. Psaltis, C. Yang, *Proc. Natl. Acad. Sci. U. S. A.* **2008**, *105*, 10670.
- [10] a) J. N. Anker, W. P. Hall, O. Lyandres, N. C. Shah, J. Zhao, R. P. Van Duyne, *Nat. Mater.* **2008**, *7*, 442; b) P. L. Stiles, J. A. Dieringer, N. C. Shah, R. P. V. Duyne, *Annu. Rev. Anal. Chem.* **2008**, *1*, 601.
- [11] a) F. De Angelis, F. Gentile, F. Mecarini, G. Das, M. Moretti, P. Candeloro, M. L. Coluccio, G. Cojoc, A. Accardo, C. Liberale, R. P. Zaccaria, G. Perozziello, L. Tirinato, A. Toma, G. Cuda, R. Cingolani, E. Di Fabrizio, *Nat. Photonics* **2011**, *5*, 682; b) X. Li, H. K. Lee, I. Y. Phang, C. K. Lee, X. Y. Ling, *Anal. Chem.* **2014**, *86*, 10437; c) T. Y. Jeon, J. H. Kim, S.-G. Park, J.-D. Kwon, D.-H. Kim, S.-H. Kim, *Adv. Opt. Mater.* **2016**, *4*, 1893; d) M. Lee, C. Mun, D.-H. Kim, S.-C. Chang, S.-G. Park, *RSC Adv.* **2016**, *6*, 92120.
- [12] a) M. A. Seo, H. R. Park, S. M. Koo, D. J. Park, J. H. Kang, O. K. Suwal, S. S. Choi, P. C. M. Planken, G. S. Park, N. K. Park, Q. H. Park, D. S. Kim, *Nat. Photonics* **2009**, *3*, 152; b) X. Chen, H.-R. Park, M. Pelton, X. Piao, N. C. Lindquist, H. Im, Y. J. Kim, J. S. Ahn, K. J. Ahn, N. Park, D.-S. Kim, S.-H. Oh, *Nat. Commun.* **2013**, *4*, 2361; c) K. V. Sreekanth, Y. Alapan, M. ElKabbash, E. Ilker, M. Hinczewski, U. A. Gurkan, A. De Luca, G. Strangi, *Nat. Mater.* **2016**, *15*, 621; d) D.-K. Lim, K.-S. Jeon, H. M. Kim, J.-M. Nam, Y. D. Suh, *Nat. Mater.* **2010**, *9*, 60; e) I. Kim, J. Mun, K. M. Baek, M. Kim, C. Hao, C.-W. Qiu, Y. S. Jung, J. Rho, *Mater. Today* **2020**, *39*, 89; f) H. Lee, I. Kim, C. Park, M. Kang, J. Choi, K.-Y. Jeong, J. Mun, Y. Kim, J. Park, M. B. Raschke, H.-G. Park, M. S. Jeong, J. Rho, K.-D. Park, *Adv. Funct. Mater.* **2021**, *31*, 2102893.
- [13] a) M. N. MacGregor-Ramiata, K. Vasilev, *Adv. Mater. Interfaces* **2017**, *4*, 1700381; b) K. Rykaczewski, W. A. Osborn, J. Chinn, M. L. Walker, J. H. J. Scott, W. Jones, C. Hao, S. Yao, Z. Wang, *Soft Matter* **2012**, *8*, 8786; c) Y. Si, Z. Guo, *Nanoscale* **2015**, *7*, 5922.
- [14] a) A. K. Yetisen, H. Butt, L. R. Volpatti, I. Pavlichenko, M. Humar, S. J. J. Kwok, H. Koo, K. S. Kim, I. Naydenova, A. Khademhosseini, S. K. Hahn, S. H. Yun, *Biotechnol. Adv.* **2016**, *34*, 250; b) I. B. Burgess, M. Lončar, J. Aizenberg, *J. Mater. Chem. C* **2013**, *1*, 6075.
- [15] a) I. B. Burgess, L. Mishchenko, B. D. Hatton, M. Kolle, M. Lončar, J. Aizenberg, *J. Am. Chem. Soc.* **2011**, *133*, 12430; b) I. B. Burgess, N. Koay, K. P. Raymond, M. Kolle, M. Lončar, J. Aizenberg, *ACS Nano* **2012**, *6*, 1427.
- [16] a) C. Chen, X. Xu, Y. Li, H. Jans, P. Neutens, S. Kerman, G. Vereecke, F. Holsteyns, G. Maes, L. Lagae, T. Stakenborg, P. van Dorpe, *Chem. Sci.* **2015**, *6*, 6564; b) J. Jeong, H. S. Yun, D. Kim, K. S. Lee, H.-K. Choi, Z. H. Kim, S. W. Lee, D.-S. Kim, *Adv. Opt. Mater.* **2018**, *6*, 1800582.
- [17] a) E.-S. Yu, S.-H. Lee, Y.-G. Bae, J. Choi, D. Lee, C. Kim, T. Lee, S.-Y. Lee, S.-D. Lee, Y.-S. Ryu, *ACS Appl. Mater. Interfaces* **2018**, *10*, 38581; b) T. Kim, E.-S. Yu, Y.-G. Bae, J. Lee, I. S. Kim, S. Chung, S.-Y. Lee, Y.-S. Ryu, *Light: Sci. Appl.* **2020**, *9*, 175; c) H.-D. Jeong, J. Lee, E.-S. Yu, T. Kim, I. S. Kim, S.-D. Lee, Y.-S. Ryu, S.-Y. Lee, *ACS Appl. Nano Mater.* **2021**, *4*, 389.
- [18] T. C. Choy, *Effective Medium Theory: Principles and Applications*, Oxford University Press, Oxford, UK **2015**.
- [19] A. B. D. Cassie, S. Baxter, *Trans. Faraday Soc.* **1944**, *40*, 546.
- [20] R. N. Wenzel, *Ind. Eng. Chem.* **1936**, *28*, 988.
- [21] W. Dai, Y.-P. Zhao, *J. Adhes. Sci. Technol.* **2008**, *22*, 217.
- [22] A. Quinn, R. Sedev, J. Ralston, *J. Phys. Chem. B* **2005**, *109*, 6268.
- [23] a) X. Chen, J. A. Weibel, S. V. Garimella, *Sci. Rep.* **2015**, *5*, 17110; b) R. Roy, J. A. Weibel, S. V. Garimella, *Langmuir* **2018**, *34*, 12787.
- [24] a) Y.-L. Yeh, *Opt. Lasers Eng.* **2008**, *46*, 666; b) H. Sobral, M. Peña-Gomar, *Appl. Opt.* **2015**, *54*, 8453.
- [25] D. R. Lide, *CRC Handbook of Chemistry and Physics*, CRC Press, Boca Raton, FL **2012**.
- [26] W. Mokrzycki, M. Tatol, *Mach. Graph. Vis.* **2011**, *20*, 383.
- [27] R. Adato, S. Aksu, H. Altug, *Mater. Today* **2015**, *18*, 436.
- [28] M. Seo, H.-R. Park, *Adv. Opt. Mater.* **2020**, *8*, 1900662.
- [29] a) A. Lafuma, D. Quéré, *Nat. Mater.* **2003**, *2*, 457; b) Z. Han, B. Tay, C. Tan, M. Shakerzadeh, K. Ostrikov, *ACS Nano* **2009**, *3*, 3031.
- [30] P. Papadopoulos, L. Mammen, X. Deng, D. Vollmer, H.-J. Butt, *Proc. Natl. Acad. Sci. U. S. A.* **2013**, *110*, 3254.
- [31] G. Wiegand, K. R. Neumaier, E. Sackmann, *Appl. Opt.* **1998**, *37*, 6892.
- [32] A. T. Paxson, K. K. Varanasi, *Nat. Commun.* **2013**, *4*, 1492.
- [33] K. Rykaczewski, T. Landin, M. L. Walker, J. H. J. Scott, K. K. Varanasi, *ACS Nano* **2012**, *6*, 9326.
- [34] T. N. Krupenkin, J. A. Taylor, T. M. Schneider, S. Yang, *Langmuir* **2004**, *20*, 3824.
- [35] R. Dufour, N. Saad, J. Carlier, P. Campistrone, G. Nassar, M. Toubal, R. Boukherroub, V. Senez, B. Nongaillard, V. Thomy, *Langmuir* **2013**, *29*, 13129.
- [36] J. C. Tuberquia, W. S. Song, G. K. Jennings, *Anal. Chem.* **2011**, *83*, 6184.
- [37] a) N. Vrancken, S. Sergeant, G. Vereecke, G. Doumen, F. Holsteyns, H. Terryn, S. De Gendt, X. Xu, *Langmuir* **2017**, *33*, 3601; b) N. Vrancken, J. Li, S. Sergeant, G. Vereecke, G. Doumen, F. Holsteyns, C. Chen, H. Terryn, S. De Gendt, X. Xu, *Sci. Rep.* **2018**, *8*, 11637.
- [38] a) X. Zhu, C. Vannahme, E. Højlund-Nielsen, N. A. Mortensen, A. Kristensen, *Nat. Nanotechnol.* **2016**, *11*, 325; b) S. Daqiqeh Rezaei, J. Ho, T. Wang, S. Ramakrishna, J. K. W. Yang, *Nano Lett.* **2020**, *20*, 4422; c) H. Liu, W. Dong, H. Wang, L. Lu, Q. Ruan, Y. S. Tan, R. E. Simpson, J. K. W. Yang, *Sci. Adv.* **2020**, *6*, eabb7171.